Measurements of the deuterium ion toroidal rotation in the DIII-D tokamak and comparison to neoclassical theory[a)]

B. A. Grierson,[1,b),c)] K. H. Burrell,[2] W. W. Heidbrink,[3] M. J. Lanctot,[4]
N. A. Pablant,[1] and W. M. Solomon[1]
[1]*Princeton Plasma Physics Laboratory, Princeton University, Princeton, New Jersey 08543, USA*
[2]*General Atomics, P.O. Box 85608, San Diego, California 92186-5608, USA*
[3]*University of California, Irvine, California 92697, USA*
[4]*Lawrence Livermore National Laboratory, Livermore, California 94551, USA*

(Received 16 December 2011; accepted 30 January 2012; published online 28 March 2012)

Bulk ion toroidal rotation plays a critical role in controlling microturbulence and MHD stability as well as yielding important insight into angular momentum transport and the investigation of intrinsic rotation. So far, our understanding of bulk plasma flow in hydrogenic plasmas has been inferred from impurity ion velocity measurements and neoclassical theoretical calculations. However, the validity of these inferences has not been tested rigorously through direct measurement of the main-ion rotation in deuterium plasmas, particularly in regions of the plasma with steep pressure gradients where very large differences can be expected between bulk ion and impurity rotation. New advances in the analysis of wavelength-resolved D_α emission on the DIII-D tokamak [J. L. Luxon *et al.*, Fusion Sci. Technol. **48**, 807 (2002)] have enabled accurate measurements of the main-ion (deuteron) temperature and toroidal rotation. The D_α emission spectrum is accurately fit using a model that incorporates thermal deuterium charge exchange, beam emission, and fast ion D_α (FIDA) emission spectra. Simultaneous spectral measurements of counter current injected and co current injected neutral beams permit a direct determination of the deuterium toroidal velocity. Time-dependent collisional radiative modeling of the photoemission process is in quantitative agreement with measured spectral characteristics. L-mode discharges with low beam ion densities and broad thermal pressure profiles exhibit deuteron temperature and toroidal rotation velocities similar to carbon. However, intrinsic rotation H-mode conditions and plasmas with internal transport barriers exhibit differences between core deuteron and carbon rotation which are inconsistent with the sign and magnitude of the neoclassical predictions. © *2012 American Institute of Physics*. [http://dx.doi.org/10.1063/1.3694656]

I. INTRODUCTION

Plasma toroidal rotation is generally considered a stabilizing mechanism for deleterious magnetohydrodynamic (MHD) instabilities such as the resistive wall mode (RWM)[1,2] and neoclassical tearing mode (NTM),[3–5] as well as contributing to $\mathbf{E} \times \mathbf{B}$ shear stabilization of turbulence[6] through the radial electric field E_r. Intrinsic rotation,[7–9] which is toroidal rotation in absence of direct momentum input, has been observed in many devices. Intrinsic rotation may play a crucial role in determining the stability and transport of future larger devices, such as ITER, with relatively low torque provided by neutral beam injection.[10]

In modern tokamaks, an impurity species is typically used for the measurement of ion temperature and plasma rotation in the toroidal and poloidal direction.[11,12] However, neoclassical theory[13–15] predicts differences between the toroidal rotation of the main ions and impurities due to finite poloidal flow and pressure gradients. In order to assess the intrinsic rotation of the bulk ion species and extrapolate to the rotation characteristics of future high performance plasmas, direct measurements of the bulk ion toroidal rotation are required.

Preliminary measurements which demonstrated the feasibility of deuterium main-ion toroidal rotation measurements in the core of DIII-D plasmas utilized a comprehensive spectral fit model which incorporated all photoemission sources, and complementary views of co and counter current directed neutral beams.[16] Subsequently, the use of a fully three-dimensional simulation of the photoemission sources, FIDAsim,[17] accurately reproduced the intensity of all processes, and magnitude of cross-section distortions reported in Ref. 16. A profile diagnostic which covers the plasma region from magnetic axis to edge has been constructed to directly test the neoclassical theory of differential toroidal rotation between bulk ions and impurities in DIII-D. Due to the convoluted nature of neutral beam attenuation, beam emission, charge exchange, and halo neutral diffusion on plasma profiles, an integrated modeling framework is employed with multiple cross-checks to eliminate errors in interpretation of the measurements.

This paper continues in Sec. II with the experimental configuration and diagnostic specifications chosen to make neutral beam induced spectroscopic measurements. Section III

[a)]Paper NI2 5, Bull. Am. Phys. Soc. **56**, 183 (2011).
[b)]Invited speaker.
[c)]Electronic mail: bgriers@pppl.gov.

provides a brief overview of the technique of charge-exchange and recombination (CER) spectroscopy for measuring ion temperature and rotational velocity, as well as the additional diagnostic information provided by the D_α spectrum. Interpretation of the measurement is aided by the unique neutral beam viewing configuration and three-dimensional atomic modeling. Measurements of ion temperature and toroidal velocity of deuterium and carbon in an L-mode discharge are presented in Sec. IV, including the demonstration of atomic corrections to the results of spectral fitting. Section V provides a brief introduction into the neoclassical theory of differential toroidal rotation between fuel ions and impurity ions. Section VI displays measurements of the intrinsic toroidal rotation of deuterium and carbon ions in H-mode plasmas heated by electron cyclotron heating (ECH). Differences in the toroidal rotation of the two ions species are evident, and discrepancies with the neoclassical predictions are exposed. Discussion of the influence of deuterium poloidal flow is presented. Section VII displays deuterium and carbon toroidal rotation in the presence of an internal transport barrier and a "notched" velocity profile near the radial region of steepest pressure gradient. Similar discrepancies with the neoclassical theory are exposed. Conclusions are provided in Sec. VIII.

II. EXPERIMENTAL CONFIGURATION AND DIAGNOSTIC SPECIFICATIONS

A multi-chord profile diagnostic used in this work was installed on the DIII-D tokamak[18] ($R = 1.66$ m, $a = 0.67$ m) for measurement of core deuterium temperature and rotation. A plan view of the tokamak and CER systems are displayed in Fig. 1 with standard operation of plasma current I_p and toroidal field B_T being counter-clockwise and clockwise, respectively, when the tokamak is viewed from above. All sixteen of the sightlines are directed in the ctr-I_p direction. The profile diagnostic views intersect neutral beams which inject both in the co-current and counter-current direction. With independent views of the co and counter beams at the same major radius, the true toroidal rotation velocity and associated charge-exchange cross section correction can be calculated,[19] and the sign and magnitude of the correction can be compared to atomic modeling. Each neutral beam has two ion sources directed at different angles, identified by "RT" and "LT" for right or left ion source. The sixteen main ion viewing chords intersect the 30° LT and 210° RT neutral beams at matched radii pairs, spanning R = 170.48 to 218.64 cm. Impurity CER channels which measure carbon emission share the same major radius values with a small elevation difference of approximately 4 cm. The neutral beams are modulated to discriminate the spatially localized "active" emission (defined in Sec. III) for determining temperature, rotation, and density, and beam modulation is a requirement for this measurement.

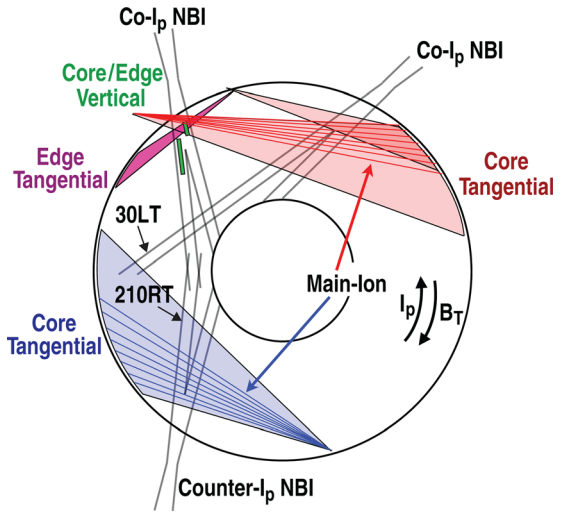

FIG. 1. Top-down view of the DIII-D tokamak displaying three neutral beam lines and CER sightlines. Viewchords of carbon (shaded) and main-ion (lines) system core viewchords indicated viewing co-I_p and counter-I_p neutral beams.

The photoemission from the tokamak is collected and focused by f/4.0 lens optics and transmitted through 1500 μm core diameter fiber to McPherson 2/3 m spectrometers. The visible light is dispersed by a 1200 g/mm grating and collected by a CCD camera which is 768 pixels wide. Each square pixel has an 18 μm width. In the first order, the spectral reciprocal dispersion is 0.180 Å/pixel. Spectral acquisition is precisely timed such that the trigger for neutral beam turn-on and CCD trigger occur simultaneously, enabling clean "timeslice subtraction," described in Sec. III. Spectra are typically obtained at integration time of 2.5 ms.

Wavelength calibration for dispersion and fiducial (zero of rotation) is performed after each tokamak discharge by using a neon calibration lamp located at the diagnostic port. Three neon lines at wavelengths 6506.5218 Å, 6532.8824 Å, and 6598.9528 Å (available from NIST) are used for shot-to-shot calibration of dispersion and wavelength fiducial of 6561.03 Å. While the dispersion does not change shot-to-shot, there can be very slight drifts in the precise fiducial location due to temperature fluctuations in the room which houses the spectrometers and CCD cameras, necessitating immediate wavelength calibration following each shot. The drift can result in as much as 1.0 km/s variation between subsequent shots if uncompensated for. Additionally, the illumination of the spectrometer from the calibration lamp differs slightly from the illumination from the beam-plasma interaction. To compensate for this, the neutral beams are fired into the tokamak pre-filled with neon gas. Neon excitation spectra from beam interaction are analyzed to determine the offset between tokamak illumination and calibration lamp illumination. The offset results in a correction of approximately 0.2 km/s. Data acquisition begins just prior to the breakdown phase of the discharge, and the first D_α spectrum of significant intensity is fit. This breakdown D_α photoemission provides further confirmation of accurate velocity fiducial, due to the breakdown emission at the rest wavelength. Finally, because the spectrometers are scannable to different wavelengths, the main-ion CER system has been tuned to the carbon C^{+6} ($n = 8 \rightarrow 7$) transition to evaluate any systematic differences between the main-ion and impurity CER systems, and none of significance has been found.

White light exposure provides the intensity response to a broadband light source and is compensated for in the spectral analysis. Absolute intensity calibration is performed with

a calibrated integrating sphere oriented inside the vacuum vessel along the neutral beam path. Absolute calibration is performed prior to plasma operations and after operational campaign with manned vessel entry.

III. IMPURITY AND MAIN-ION CHARGE EXCHANGE RECOMBINATION SPECTROSCOPY

Measurement of plasma toroidal rotation on many devices is accomplished by high power neutral beam injection enabling a technique known as CER spectroscopy.[11,12] CER which employs intrinsic impurities is used due to the relative simplicity of the spectrum near the transition wavelength and short lifetime of the excited states. On the DIII-D tokamak, the fully stripped impurity carbon C^{6+} ($n = 8 \rightarrow 7$) transition spectrum near 5290.50 Å is dominated by two Gaussian shapes which represent the cold edge and hot core. This two-Gaussian shaped spectrum can be reduced to a single Gaussian by modulation of the neutral beams and performing timeslice subtraction, removing the "passive" edge emission and obtaining the spatially localized "active" emission isolated to the region of the plasma where the viewchord and neutral beam cross. Here, we define "passive" emission as emission from the plasma edge and "active" emission following charge capture from a beam neutral to thermal ion. The "active" emission is obtained by taking the difference between the spectrum acquired when the beam is on and when the beam is off, eliminating the passive contribution to the photoemission.

Fitting of the charge-exchange spectrum results in an *apparent* temperature and velocity from the Doppler width and line shift that is different from the true temperature and velocity, due to the energy dependence of the charge-exchange cross-section.[20,21] The cross-section effect results in a false line-shift which scales with the ion temperature and with the viewing angle with respect to the neutral beam. The measured apparent velocity can be represented as $\mathbf{V}_{app} = \mathbf{V}_{true} + \alpha \hat{\mathbf{V}}_{beam}$, where α is a scalar quantity which depends on the atomic cross-section and ion temperature, and $\hat{\mathbf{V}}_{beam}$ is the unit vector along the neutral beam. Correcting for atomic physics considerations on toroidal and poloidal flow measurements has become standard practice in modern tokamaks and the reader is referred to the following Refs. 11 and 19–25.

In contrast to the impurity spectrum, the spectrum near the D_α $n = 3 \rightarrow 2$ transition of 6561.03 Å contains seven complex features with distinct physical origins. Photoemission from the tokamak edge contains bright "passive" emission from (1) cold electron impact excited edge neutral gas outside the scrape-off-layer (SOL), (2) warm edge emission inside the SOL due to charge-exchange with thermal neutral deuterium, as well as (3) two impurity lines of CII. The SOL is the region between the last closed flux-surface and the vacuum vessel with a large neutral deuterium gas concentration, and emission from (1) and (2) can be minimized by a large gap between the separatrix and the vessel wall, as well as reduced gas fueling. The temperature range of the edge emission is significantly lower than inside the plasma and the emission occurs near the rest wavelength of the atomic transition, thus being distinguished from the "active" emission. The "active" photoemission from the plasma interior associated with neutral beam injection contains (4) direct charge exchange (DCX) emission between the beam neutrals and the thermal deuterium ions, (5) "halo"[17,26,27] neutral emission from the excited product of charge-exchange between the direct charge-exchange thermal neutral and thermal ions, (6) charge exchange emission between the beam and fast ions D_α (FIDA), as well as (7) emission from the beam neutrals themselves. Direct charge-exchange and halo charge-exchange emission appear as a single feature in the observed spectrum. The former is distorted by the energy dependence of the charge-exchange cross-section, and the latter emits with the true local plasma temperature and rotation velocity, *albeit* from a slightly larger spatial volume due to spatial diffusion before ionization. The general effect of the halo is to reduce the *magnitude* of the apparent velocity shift away from the true velocity. The D_α spectrum presents an enormous amount of information which can be exploited for its diagnostic potential and displays in excess of 30 spectral features which need to be fit self-consistently.[26]

An example of the D_α spectrum and complete fit is presented in Fig. 2. This is a view of the co-I_p beamline 30 LT in an L-mode discharge with line averaged electron density 2×10^{19} m^{-3}, central ion temperature of 1.5 keV, and toroidal rotation near 5 km/s. The largest feature is the thermal charge-exchange emission, which is fit by a single Gaussian shape convolved with the instrumental function. The thermal charge exchange emission contains the bulk temperature, apparent velocity and density through the width, line shift, and intensity of the Gaussian. Spectral fitting is performed in pixel, rather than wavelength. The temperature of the emitting ion is $T_i = \frac{1}{2} mc^2 (Dw/\lambda_0)^2$, where m is the ion mass, c is the speed of light, w is the Gaussian width, D is the spectrometer reciprocal dispersion (Å/pixel), and λ_0 is the rest

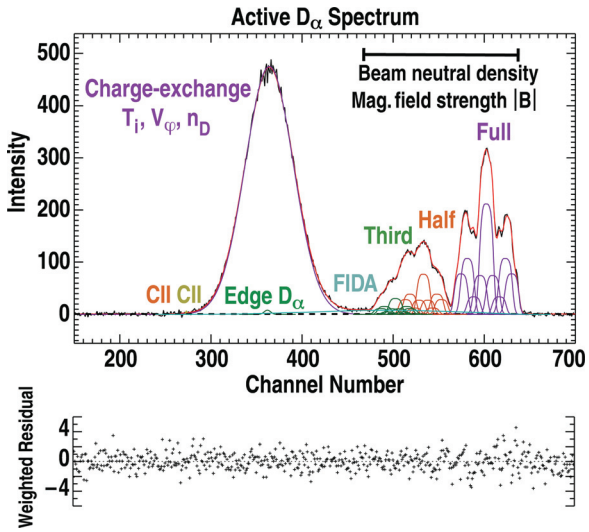

FIG. 2. Complete fit to active D_α spectrum obtained by timeslice subtraction. The fit model incorporates the thermal charge-exchange feature localized between channels 280–450, beam emission of 81 kV injection indentified as full, half, and third, fast-ion emission (FIDA) and small contributions from edge D_α and carbon (CII). The spectral data are displayed in black and sum of all contributions displayed in red. The low amplitude and uniform weighted residuals is characteristic of a high quality fit.

wavelength of the atomic transition. The line-of-sight (LOS) apparent velocity is computed by $V_{los}^{app} = c\Delta pD/\lambda_0$, where Δp is the difference between the fit pixel value and the fiducial pixel value at 6561.03 Å. The toroidal velocity V_{φ}^{app} is computed by dividing the LOS velocity by the cosine of the angle the viewchord makes with the toroidal direction at the beam crossing.

The second largest feature is the beam emission which is fit using the B-Stark model, detailed in Refs. 28–30. The beam emission fit contains the beam neutral density of the three energy components (full, half, and third), as well as the local magnetic field strength $|B|$ determined by the linear wavelength separation of the Stark multiplet.

The third most intense feature originates from injected fast ions which pass through the beam and halo neutrals, recombine, and emit a D_α photon. This FIDA emission has received considerable interest in studies of fast-ion transport by Alfvén modes and turbulence.[31,32] FIDA emission is incorporated into the spectral fit model through TRANSP (Refs. 33 and 34) and NUBEAM (Ref. 35) production of the fast ion distribution function. The distribution function from NUBEAM is used as input to a three-dimensional, time-dependent collisional-radiative modeling code FIDAsim, detailed in Ref. 17. FIDAsim uses the complete experimental configuration, including neutral beam source geometry and sightlines across the vessel through the neutral beam. The code requires equilibrium fitting code (EFIT) (Ref. 36) equilibrium reconstruction, kinetic profiles of electron density and temperature, ion temperature, toroidal rotation, fast ion distribution, and impurity density. The code performs neutral beam attenuation and emission calculations, direct charge-exchange and emission, halo neutral production and spatial diffusion and emission, as well as fast-ion charge-exchange and emission. The FIDA spectral shape is used in the fitting procedure at a fixed central wavelength, and amplitude of the FIDA shape displayed in Fig. 2 is a free parameter. Previous work[37] on FIDA modeling indicated that the amplitude varied much more strongly than the shape of the emission spectrum in a wide variety of conditions; and therefore, modifications to the fast-ion distribution function will impose a weak influence on the fit to the thermal charge exchange features when the FIDA amplitude is un-constrained.

The final fitting step is to allow for small remaining edge localized features which were not subtracted out perfectly. The contributions from the edge are highly constrained to be cold and emit near the rest wavelength of the atomic transition. As displayed in Fig. 2, the negligible intensity of the edge emission gives confidence that the spectral features being fit originate from deep inside the plasma uncorrupted from the edge light.

A. Necessity of a fast-ion model

In plasma with low beam power (Fig. 2) and/or very high density, the intensity of the FIDA contribution may be nearly negligible, but is still included in the spectral fit to eliminate systematic errors. However, in plasmas with high beam power, the FIDA contribution can be significant. Displayed in Fig. 3 is a comparison of spectral fits when the FIDA emission is omitted from the fit model, Fig. 3(a), and when the FIDA contribution is included in the fit model Fig. 3(b). The view displayed in Fig. 3 is of a ctr-I_p beam, such that the beam emission from the 210 RT beamline and the fast-ion emission from the co-I_p injected fast ions are on opposite sides of the thermal Gaussian. It is clear from Fig. 3(a) and examination of the weighted residual error that the fit model is lacking a significant source of emission, and the residual is unacceptably high. Comparison of the thermal Gaussian properties between Figs. 3(a) and 3(b) indicates that a difference in apparent ion temperature of approximately 0.1 keV and an apparent velocity difference of 8 km/s would be incurred if the FIDA emission were neglected, which is an unacceptably high error.

B. Quantitative comparison of measured and modeled emission

Due to the convoluted nature of the attenuation of the three primary beam components on plasma profiles of electron and ion densities, and subsequent charge-exchange with fuel ions and impurities, it is necessary to establish reasonable agreement with all measured photoemission processes. The injection of beam neutrals begins the process which leads to charge-exchange emission, and hence must be modeled accurately. The emission intensity from the beam neutrals is proportional to the beam neutral density, $I^{BES(j)} = q^{eff}(v_j)n_{eff}n_b^{(j)}$,

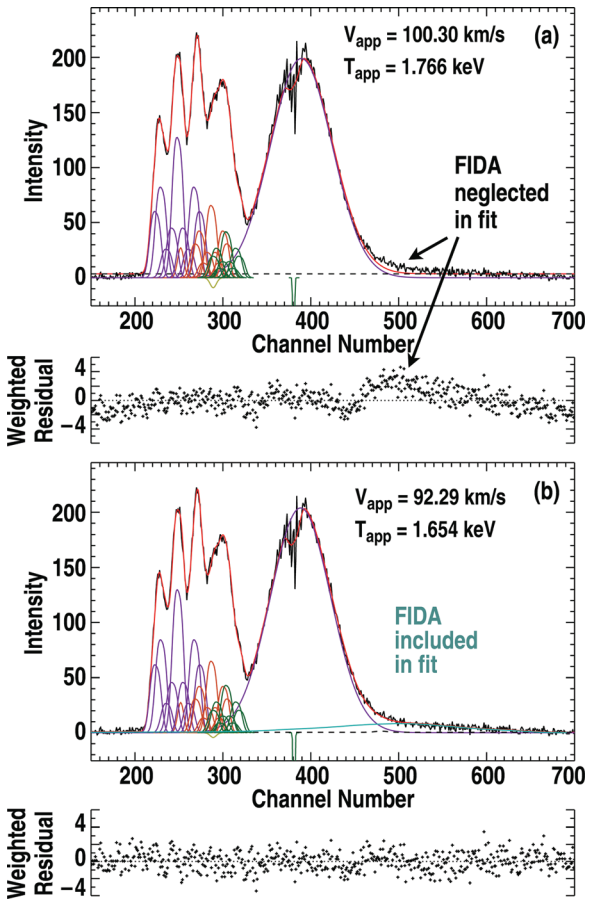

FIG. 3. Comparison of spectral fitting when (a) FIDA is neglected and (b) when FIDA is included. Neglecting the FIDA emission results in a poor quality fit. Colors same as Fig. 2.

where q^{eff} can be thought of as an effective excitation coefficient, n_{eff} represents the target density of electrons and ions, n_b is the beam neutral density, and j denotes beam species.[38] In the FIDAsim code, beam neutral density attenuation from each plasma constituent (electron, fuel ion, and impurity ionization) is computed separately, foregoing effective beam stopping rates used in the automatic data acquisition system (ADAS) (Ref. 39) package. Beam emission is determined from the fraction of beam neutrals in the excited $n = 3$ state.

Having performed the beam attenuation calculation with FIDAsim, the processes of charge-exchange with fuel ions yields the direct charge-exchange photoemission and neutral diffusion produces the halo. Subsequently, fast-ion charge-exchange between both beam neutrals and halo neutrals is calculated. Both the direct charge-exchange and fast-ion charge-exchange are done via time-dependent collisional radiative modeling. It is, therefore, necessary that all processes be modeled accurately and self-consistently. This is primarily important for interpretation of the FIDA emission, because the penalty is two-fold when the beam attenuation (fast-ion deposition) is computed inaccurately, resulting in an erroneous fast-ion density, and subsequent FIDA emission (proportional to the product of fast-ion density and beam neutral density).

Displayed in Fig. 4 are profiles of FIDA emission intensity, beam emission intensity, and fractional beam neutral density across the plasma minor radius for three times in a discharge. Over the time range of 1280-1880 ms, the electron density ramped from $2.5 - 6.7 \times 10^{19}\,\mathrm{m}^{-3}$ as the discharge entered H-mode. TRANSP analysis of plasma evolution and NUBEAM fast ion distribution function was used as input to the FIDAsim code. Measured and calculated neutron rates from TRANSP were matched and the fast-ion confinement was approximately classical. Overplotted as broken lines in the figure are the results from FIDAsim modeling of each emission process. In Figs. 4(a)–4(c) (top), it can be seen that the FIDA emission intensity is peaked in the plasma core at low density, becomes flat at moderate density, and changes slope at the highest density. At very high density, the beam can no longer penetrate effectively into the core, and the fast ion slowing down time is abbreviated considerably, such that the strength of the FIDA emission is greatly reduced. The beam power was constant throughout the times displayed here, as such the evolution of the FIDA profile is due to changes in fast-ion deposition, Coulomb scattering and slowing down, and neutral beam attenuation as the density increases. Figures 4(a)–4(c) (middle) display the beam emission intensity. At low density, the beam emission is approximately a linearly decreasing function into the core. Figure 4(b) (middle) displays the increase in beam emission at the plasma edge as the H-mode pedestal is formed, being a target rich volume for collisional excitation, and an exponential character to the attenuation into the core. By 1880 ms, Fig. 4(c) (middle), the plasma density profile causes strong attenuation all the way into the core and the lower velocity half and third energy contributions have been strongly attenuated. Figures 4(a)–4(c) (bottom) displays the variation of neutral beam density fractions of full, half, and third energy, which are computed from measured emission intensity and excitation cross-sections. Accurate beam density fractions are required for evaluation of the charge-exchange cross-section effect, which is a sum over beam fractions.[21] As the plasma density increases, the beam neutral density becomes strongly dominated by the full energy component which has much better penetration. Additionally, the baseline visible bremsstrahlung (VB) level (not shown) is in very good agreement with that expected from line-integrated calculations.

Spectral data and FIDAsim spectra output can also be compared directly. Figure 5 displays all active photoemission processes which contribute to the complete D_α spectrum at R = 1.84 m in Fig. 4(b). The halo and DCX are added together to produce the total thermal charge exchange Gaussian (Halo + DCX), which matches very well to the experimentally measured spectrum. The beam emission shape in Fig. 5 does not take into account the instrumental broadening and no effort is made to reproduce the details of

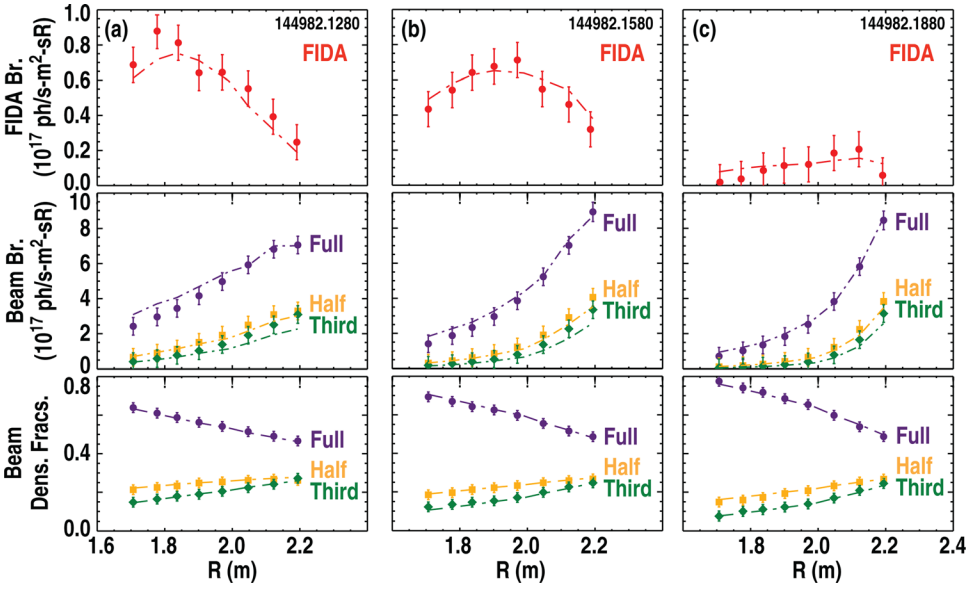

FIG. 4. Profiles of absolute brightness FIDA D_α emission intensity, beam D_α emission intensity, and beam neutral density fractions for three times as the plasma density is ramped from (a) 2.5, (b) 4.5, and (c) 6.7×10^{19} m^{-3} at fixed beam power. Broken lines indicate modeled emission from FIDAsim.

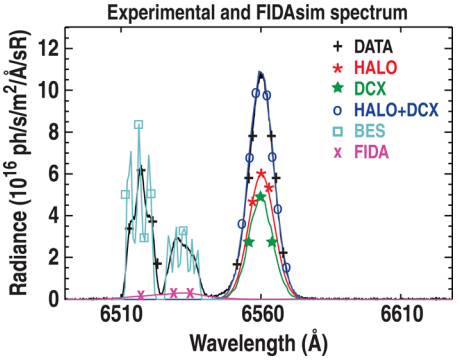

FIG. 5. Comparison of active spectral data with forward modeling with the FIDAsim. The sum of halo and DCX intensity is in good agreement with the experimentally measured thermal spectral radiance.

the $n = 3$ level populations,[40] however the total wavelength integrated radiance (brightness) is in good agreement.

IV. DETERMINATION OF BULK ION TOROIDAL ROTATION IN L-MODE DISCHARGE WITH BROAD PRESSURE PROFILE

A low confinement (L-mode) discharge in DIII-D has been investigated using the main-ion CER diagnostic to demonstrate the measurement of the thermal deuterium temperature and toroidal rotation profile. Spectral measurements of both co and counter neutral beam injection were obtained during steady conditions. Some parameters of interest were the values of plasma current $I_p = 1.0$ MA, toroidal magnetic field $B_T = -2.0$ T and line-averaged density 2.1×10^{19} m^{-3}. The plasma shape was lower single null (LSN) with a large outer gap of approximately 12 cm. A large outer gap and no gas fueling are favorable for main-ion CER to minimize the plasma-wall interaction and reduce the bath of edge neutrals for collisional excitation and bright edge emission.

Active spectra for all sixteen viewchords were fit using the method described in Sec. III, and the results averaged over a period of 20 ms are displayed in Fig. 6. The profile Fig. 6(a) shows the carbon temperature from a spline fit representation, as well as the temperature from the co-I_p and ctr-I_p viewing main-ion CER system. The apparent velocity profile is displayed in Fig. 6(b). Two distinct temperature profiles are observed, where the co-I_p viewing system reports a temperature which is slightly lower than the ctr-I_p viewing system. The co-I_p viewing system has a larger angle from perpendicular with respect to the neutral beam injection, and thus the spectrum exhibits a larger cross-section distortion. In a similar manner, the apparent velocity profiles display two well separated profiles. The true rotational velocity always lies between the two apparent velocity profiles and is closer to the ctr-I_p viewing chords due to the more perpendicular angle. Further, examination of the difference between apparent velocities from co-I_p and ctr-I_p views scales with ion temperature. Apparent velocity differences $V_{app}^{co} - V_{app}^{ctr}$ are larger where the temperature is higher, nearly 10 km/s in the core, and smaller, 2–3 km/s at the plasma edge, and this is a general trend. Figures 6(c) and 6(d) display the profiles which have been corrected for atomic physics distortions. The ion temperature of carbon and deuterium are in good

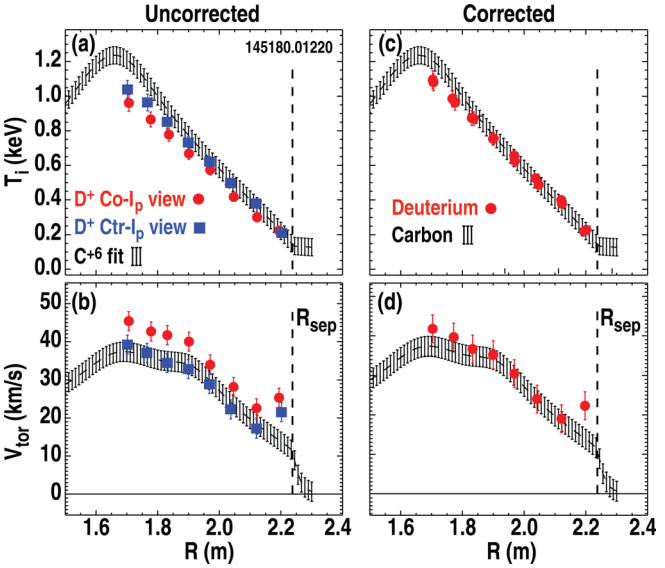

FIG. 6. Determination of deuterium temperature and toroidal rotation by correcting apparent values. (a) and (b) Profiles of apparent temperature and velocity from both co-I_p and ctr-I_p viewing D_α systems, and spline fit of carbon temperature and carbon corrected velocity. (c) and (d) Profiles of corrected temperature and toroidal velocity, and carbon profiles [same as (a) and (b)].

agreement, as expected from the rapid thermal equilibration between species on the order of micro-seconds under these conditions. Additionally, the toroidal rotation between species is quite similar across the profile in this low temperature L-mode discharge, except for the value near the separatrix. Near the separatrix, the deuterium flow speed can greatly exceed that for carbon. This edge co-I_p rotation layer of the main-ions has been measured by Mach probes in DIII-D in a variety of conditions[41–43] and can approach 80 km/s in both L-mode and H-mode discharges.

Temperature scaling of the cross-section effect has been investigated in similar conditions (but not the same discharge as Fig. 6), where the ion temperature varied from 1.0 to 2.0 keV. Presented in Fig. 7 is the difference between apparent velocities for two views at matched radius. It is clear that the difference in apparent velocities increases at higher temperature, in qualitative agreement with expectations. The co-I_p viewing system always measures apparent velocities which

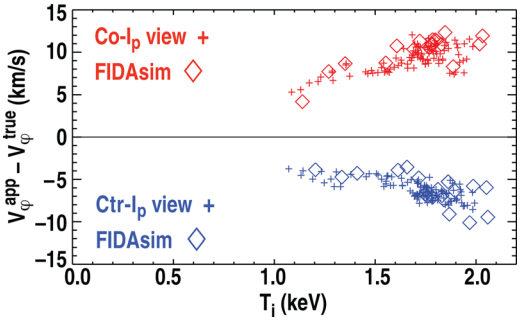

FIG. 7. Variation of the apparent velocity correction for matched co and counter viewchords as the ion temperature is increased. At higher temperatures, the difference between apparent velocities from co and counter viewing systems becomes large.

are "faster" in the toroidal direction than the true velocity. The ctr-I_p viewing system always measures apparent velocities which are "slower" in the toroidal direction than the true velocity. Further, the scaling of the ctr-I_p view is weaker than the co-I_p view, because the ctr-I_p views are more perpendicular to the neutral beam injection. Also included in Fig. 7 is the apparent velocity correction as estimated by the FIDAsim code. It is clear that the FIDAsim code is accurately capturing the sign and magnitude of the energy dependent cross-section correction.

V. NEOCLASSICAL THEORY OF DIFFERENTIAL TOROIDAL ROTATION BETWEEN TWO ION SPECIES

Flow velocities in tokamaks are characterized by the vector components in the toroidal and poloidal directions. Here, toroidal is defined by the angle φ in the right-handed coordinate triad of major radius, azimuthal angle and elevation R, φ, z, where $\hat{R} \times \hat{\varphi} = \hat{z}$, and $\hat{\varphi}$ is the standard direction of plasma current in the discharges reported here, $I_p > 0$. The toroidal magnetic field is in the opposite direction to the plasma current, $B_T < 0$. With the origin at the magnetic axis, the coordinates of r, θ, φ define the minor radius, poloidal angle, and toroidal angle such that $\hat{r} \times \hat{\theta} = \hat{\varphi}$, and $\hat{\theta}$ is in the direction of gravity on the outboard midplane $(-\hat{z})$, and the direction of the poloidal field for the standard direction of the plasma current, $B_\theta > 0$. The plasma flow velocities are related to each other by the pressure gradient and electric field in the radial force balance relation

$$E_r = \frac{\nabla P_i}{Z_i e n_i} + V_\varphi B_\theta - V_\theta B_\varphi, \tag{1}$$

where here any ion species can be used. Construction of the radial electric field from experimental CER data can be performed by direct measurements of the carbon toroidal and poloidal velocity, temperature, density and equilibrium reconstruction of the magnetic fields.

Poloidal flow in tokamaks is driven by thermodynamic forces and is strongly damped due the variation of magnetic field strength around one poloidal transit. In the neoclassical treatment, the direction of the poloidal flow can vary depending on the collisionality regime of the ions species[14] and arises on the ion-ion collision timescale. Low collisionality banana regime poloidal flow of the main-ions is in the ion diamagnetic direction for the configuration considered here, where $\mathbf{B} \times \nabla P$ is in the positive poloidal direction,[44,45] although the sign convention is different in Ref. 44 from this article. Poloidally passing ions carry the net flow velocity, and collisional friction with banana trapped ions determines the direction of the net flow. In higher collisionality regimes of plateau and Pfirsch-Schlüter, poloidal flow is in the opposite direction. A simplified expression for the main-ion poloidal flow velocity in a pure plasma can be expressed as[44]

$$V_\theta = \frac{k}{m_i \Omega_i} \frac{dT_i}{dr}, \tag{2}$$

where k is equal to 1.17, −0.5, and −1.7 in the banana, plateau, and Pfirsch-Schlüter regimes, respectively, m_i is the ion mass, $\Omega_i = Z_i eB/m_i$ is the ion cyclotron frequency which carries the sign of B, T_i is the ion temperature, and r is the minor radius. Thus, in standard configuration in DIII-D with banana regime bulk ions and a monotonically decreasing temperature profile, the main-ion poloidal flow is in the positive poloidal direction (both Ω_i and the temperature gradient are negative). Previous investigations into bulk ion poloidal flow in helium discharges confirmed this directionality in the H-mode edge,[45] although the magnitude was in strong disagreement with neoclassical estimates. It is of note that reversing the sign of the toroidal field will reverse the sign of the poloidal flow in the neoclassical treatment.

Direct poloidal velocity measurements of impurity carbon have been the subject of much scrutiny due to the high accuracy required for the measurement of a small poloidal velocity in the face of a much larger toroidal velocity (and toroidal "pickup"), and the complexity of the energy dependent process by which a gyrating carbon ion captures a charge from the beam neutral, undergoes some fraction of a gyro orbit, and emits radiation.[22,24,46] Comparisons of measured carbon poloidal flow and neoclassical theory have shown a mix of reasonable agreement[47,48] and large disagreement.[46,49,50] The primary employment of the neoclassical theory resides in the computation of the poloidal flow velocity for comparison to experimental measurements, or completion of Eq. (1) when direct measurements of V_θ are unavailable.

After computation of the poloidal flow of the main ion species, the difference between the toroidal flow of the main (deuterium) ions and carbon impurity ions can be computed by noting that the radial electric field is the same for both species; $E_r^D = E_r^C \equiv E_r$. Re-arrangement of Eq. (1) for deuterium and carbon ions results in the expression

$$V_\varphi^D = V_\varphi^C + \frac{1}{B_\theta}\left(\frac{\nabla P_C}{Z_C e n_C} - \frac{\nabla P_D}{Z_D e n_D}\right) + \frac{B_\varphi}{B_\theta}\left(V_\theta^D - V_\theta^C\right), \tag{3}$$

where D and C indicate deuterium and carbon, respectively. Examination of Eq. (3) reveals that for small poloidal flow, and noting the $1/Z_C$ dependence of the carbon pressure term, that the deuterium ion toroidal rotation should be more positive in the toroidal direction than carbon $(V_\varphi^D - V_\varphi^C) > 0$ and scale with the main-ion pressure gradient, sign, and magnitude of the poloidal field. In this limit, reversing the sign of the plasma current will reverse the sign of $(V_\varphi^D - V_\varphi^C)$. Contributions from the poloidal flow can be large if there is a large differential poloidal rotation between carbon and deuterium. For the configuration considered in this article, B_φ is negative, hence a large positive deuterium poloidal flow with low carbon flow velocity can reduce the positive contribution from the main-ion pressure in Eq. (3), and even reverse the sign of $(V_\varphi^D - V_\varphi^C)$.

In practice, computer codes such as NCLASS,[15] NEO (Ref. 51), and GTC-Neo[52] are used to evaluate the thermodynamic forces and collisionality using a treatment which spans all aspect ratios and collisionality regimes continuously. The inputs to the code are the EFIT (Ref. 36) reconstructed magnetic equilibrium, and profiles of electron density n_e and temperature T_e here measured by Thomson scattering and

electron-cyclotron emission. The ion temperature T_i^C, toroidal rotation V_φ^C, and impurity density n_C are calculated from carbon CER. Thermal deuterium is assumed to have the same temperature as the measured carbon ions such that $T_i^D \equiv T_i^C$. The thermal deuterium density is computed by quasi-neutrality where $Z_D n_D = n_e - (Z_C n_C + Z_D n_{fast})$, and here the fast ions contribute only charge density and are removed from consideration. In these codes, no treatment is given of the effects of the presence of fast ion pressure, transport, or collisional friction with the bulk ions or impurities.

It is noteworthy that additional physics such as turbulence, neoclassical toroidal viscosity (NTV), detailed flow damping through charge-exchange, and MHD instabilities are not considered in the neoclassical collisional theory. Effects of turbulent transport on ion thermal conductivity and momentum diffusivity dominate over neoclassical effects in many experimental investigations and gyro-kinetic treatments of turbulence effects on poloidal flow are being investigated.[53,54]

VI. INTRINSIC ROTATION OF BULK IONS IN ECH H-MODE

Intrinsic rotation is defined as the nonzero plasma toroidal rotation in absence of known direct momentum input. Databases of intrinsic rotation scaling have been compiled by Rice *et al.*[8] and show the general trend of a positive incremental rotation change from low to enhanced confinement as a function of the plasma stored energy normalized by plasma current. Intrinsic rotation studies are typically carried out using impurity toroidal rotation measurements from CER or crystal x-ray spectrometers.[55] In select cases, helium main-ion plasmas have been used to investigate the toroidal rotation of the bulk species.[7,45] Kim *et al.*[45] examined the toroidal rotation of helium ion at the plasma separatrix and exposed a strong co-I_p rotation layer of the bulk ions near the plasma boundary. This observation has been seen in deuterium plasmas as well, namely Fig. 6(d) in the present article and Mach probe measurements on DIII-D,[41–43] and may be explained by thermal ion orbit loss near the separatrix.[56] In the core region, however, measurements of helium and carbon rotation have displayed disagreement with the neoclassical ordering of $V_\varphi^{He} > V_\varphi^C$. In Ref. 7, repeat discharges were used to first measure the carbon intrinsic toroidal rotation profile, and subsequently the helium intrinsic toroidal rotation profile. Helium main-ion plasmas displayed toroidal rotation in the ctr-I_p direction over much of the core and the helium toroidal rotation was more ctr-I_p than carbon, in disagreement with the neoclassical prediction.

In the present study, utilizing the new main-ion CER system, simultaneous measurements of the carbon and deuterium toroidal rotation are made across the core profile. A sequence of discharges were executed to examine the L-mode and H-mode intrinsic rotation characteristics of deuterium bulk ions, and the carbon intrinsic impurity. ECH was applied to LSN discharges in standard I_p and B_T configurations (favorable ∇B) to enable H-mode access with approximately 0.9 MW of ECH heating. The plasma current was $I_p \approx 0.93$ MA and the toroidal field $B_T \approx -1.6$ T. The CER measurements require short "blips" of balanced neutral beam injection (NBI) from both co-I_p and ctr-I_p directed beams. During the short duration of the NBI, the injected fast ions are collisionless and do not impart a slowing-down collisional torque on the plasma. The use of balanced NBI is required to make the complementary CER measurements from the co-I_p and ctr-I_p beams, as well as null the "prompt torque" delivered by fast radial current injection.[57]

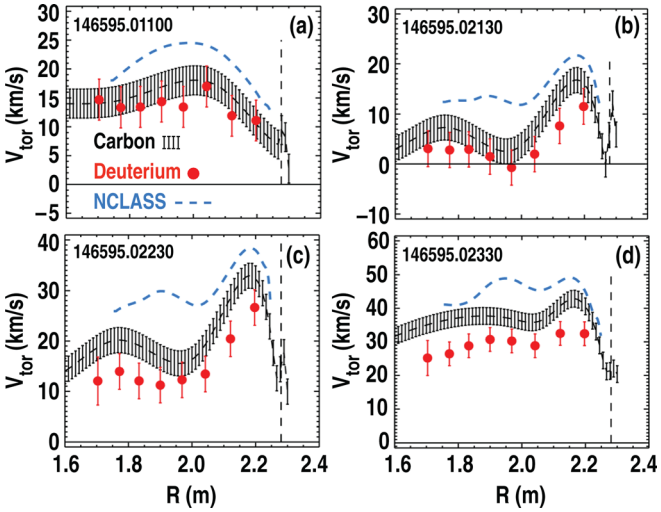

FIG. 8. Evolution of intrinsic rotation profiles of carbon and deuterium, as well as neoclassically predicted deuterium rotation (broken line). (a) L-mode rotation profile prior to application of ECH. (b) and (d) Evolution of intrinsic rotation in ECH H-mode prior to first ELM. Dashed vertical line indicates radius of separatrix on outboard midplane.

Displayed in Fig. 8 is the evolution of the rotation profile at four times in a discharge with corresponding temperature profiles in Fig. 9. Figure 8(a) displays the L-mode rotation profile of carbon and deuterium at 1100 ms into the discharge, 100 ms after the current flat-top. At 1100 ms, the line averaged density is $n_e \approx 2.2 \times 10^{19}$ m^{-3} and central $T_e \approx T_i \approx 1.0$ keV. Also displayed in Fig. 8(a) is the neoclassically predicted toroidal rotation of deuterium from the

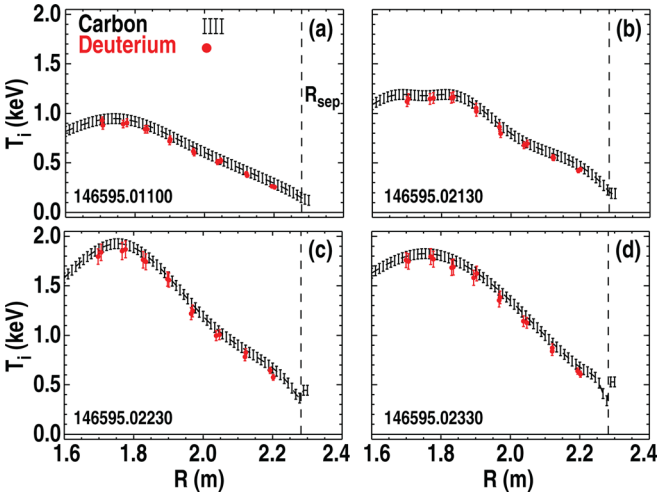

FIG. 9. Evolution of ion temperature profiles of carbon and deuterium associated with Fig. 8. (a) L-mode temperature profile prior to application of ECH. (b)-(d) Evolution of ion temperature in ECH H-mode prior to first ELM. Dashed vertical line indicates radius of separatrix on outboard midplane.

NCLASS code. It can be seen that the rotation of carbon and deuterium are nearly indistinguishable within the error estimates. At 2000 ms into the discharge, ECH is applied to trigger the transition to H-mode. The L-H transition occurs at 2080 ms, indicated by a drop in edge D_α. Displayed in Figs. 8(b)–8(d) and 9(b)–9(d) are sequential profiles every 100 ms beginning at 2130 ms into the discharge, all prior to the first edge-localized mode (ELM). In all cases, the measured deuterium ion temperature in Fig. 9 is in reasonable agreement with carbon. At 2130 ms, Fig. 8(b) clearly shows a "hollow" rotation profile for both carbon and deuterium, with the largest velocity just inside the plasma boundary. The neoclassically predicted deuterium rotation profile is more co-I_p than carbon, however the measured deuterium rotation is slightly, but systematically, more ctr-I_p than carbon. The neoclassical prediction indicates that the largest difference between deuterium and carbon should be near major radius of $R \approx 1.90$ m with a magnitude of 10 km/s, which is the location of the largest temperature gradient [$\nabla_r T_i \approx -2.2$ keV/m, Fig. 9(b)], however this difference is not observed. As the H-mode evolves, the entire rotation profile of both carbon and deuterium increase in the toroidal direction. Figure 8(c) displays the rotation profiles at 2230 ms into the discharge, where the ion temperature has risen to approximately $T_i \approx 1.9$ keV. The deuterium toroidal rotation is persistently more ctr-I_p than carbon, even though the neoclassical theory predicts a much larger rotation difference between the ion species. In Fig. 8(c), the difference between the neoclassically predicted deuterium rotation and the measured deuterium rotation has reached 20 km/s at major radius R = 1.9 m and is well outside of reasonable error estimates. It is of note that the cross-section corrections at this temperature are well below the neoclassically predicted difference in carbon and deuterium rotation. At 2330 ms in Figs. 8 and 9(d), just prior to the first ELM, the rotation profile of both species has become nearly flat. Again there remains a difference between ion species' toroidal rotational velocity which does not match the neoclassical values.

L-mode and H-mode toroidal rotation characteristics of deuterium and carbon are displayed in Figs. 6(d), 8(a), and Figs. 8(b)–8(d), respectively. In L-mode conditions, the toroidal rotation of carbon and deuterium appear nearly indistinguishable in the core. However, in H-mode intrinsic rotation conditions, the core rotation of the two ion species are different. Further detailed measurements of the intensity of turbulent fluctuations in the two regimes are warranted.

The evolution of the intrinsic rotation profile displays a general trend similar to the Rice scaling, in that the H-mode central rotation increases by approximately 30 km/s as the plasma stored energy increases (at fixed current) from 0.13 to 0.38 MJ prior to the first ELM. However, the magnitude of the bulk rotation is persistently "slower" in the co-I_p direction than carbon, not "faster" as the neoclassical theory predicts. Therefore, the scaling of intrinsic rotation databases which use impurities ions may be considered an optimistic upper limit for extrapolations to future, larger devices. Characterization of the intrinsic rotation differences between bulk deuterium ions and carbon across operational regimes is the subject of ongoing research efforts.

A. Measurement of thermal deuterium density profile

In order to accurately apply the neoclassical theory described in Sec. V, it is necessary to confirm that there are only two primary ion species with well-known density profiles. When impurity measurements are used to deduce ion density, an iterative deduction of the neutral beam density and impurity density is employed due to the convoluted dependence of beam stopping and charge-exchange emission. Figure 10 displays the profiles of the plasma density constituents at the same time as Figs. 8(a) and 9(a). Here, we have used the measured thermal deuterium photoemission intensity and the FIDAsim code to determine the bulk ion density associated with the thermal main-ion brightness. Figure 10 contains the electron density, carbon density, and bulk deuterium density from quasi-neutrality ($n_D = n_e - 6n_C$). As this was the first beam pulse, there is negligible fast-ion density and it is taken to be zero. Also included in Fig. 10 is the thermal deuterium density measured by the main-ion CER system for both co-I_p and ctr-I_p systems. It is clear that the plasma is composed of three primary constituents without other impurities or significant fast ion density from neutral beam injection, and that the density profiles of carbon and thermal deuterium are being captured accurately.

B. Inference of main-ion poloidal velocity

On examination of Eq. (3), it is clear that every term is being either directly measured, or confirmed to be consistent with observations, save one; the main-ion poloidal flow velocity. Algebraic re-arrangement of Eq. (3) yields the equation for the main-ion poloidal flow,

$$V_\theta^D = V_\theta^C - \frac{1}{B_\varphi}\left(\frac{\nabla P_C}{Z_C e n_C} - \frac{\nabla P_D}{Z_D e n_D}\right) + \frac{B_\theta}{B_\varphi}\left(V_\varphi^D - V_\varphi^C\right), \quad (4)$$

where all quantities on the right-hand side of this equation are measured. This expression permits the calculation of the deuterium poloidal flow velocity which is consistent with observed deuterium toroidal flow velocity, as it cannot be measured directly. Direct measurement of the deuterium ion poloidal flow in deuterium neutral beam heated discharges by vertical spectroscopic sightlines are hindered by the

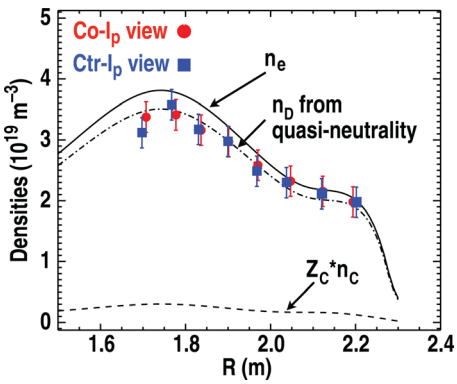

FIG. 10. Density profiles of electrons, thermal deuterium, and fully ionized carbon at the same time as Figs. 8 and 9(a) in the L-mode phase of the discharge.

presence of the bright beam emission overlapping the thermal emission. Vertical viewchords for poloidal velocity measurements are perpendicular to the neutral beam, and the beam D_α emission is not Doppler shifted away from the thermal line emission, making spectral analysis unfeasible.

The rotation profile in Fig. 8(b) and deuterium ion collisionality has been evaluated to extract the deuterium poloidal flow. Figure 11(a) displays the ion collisionality and the boundaries of the three regimes, namely the low collisionality "banana" regime, the intermediate "plateau" regime, and the high-collisionality "Pfirsch-Schlüter" regime. The collisionality regime is defined as the ratio of ion-ion collision frequency to bounce frequency, $\nu_{*,i} = \nu_i Rq/\epsilon^{3/2} v_{Ti}$, where ν_i is the ion-ion collision frequency, R is the major radius, ϵ is the inverse aspect ratio, q is the safety factor, and v_{Ti} is the ion thermal speed. The main ions are in the banana regime across the entire profile. Displayed in Fig. 11(b) are poloidal velocities. In dash-dot is the computed poloidal flow with the NCLASS code, the solid black curve displays the use of Eq. (4), and the dashed black curve is the banana regime limit of Eq. (2). Although the main-ions are well into the banana regime, where the primary ion flow should be in the ion diamagnetic direction, the approach used in NCLASS evaluates the primary ion flow to be in the opposite direction over much of the plasma minor radius. The banana regime limit of Eq. (2) provides a more accurate representation of the inferred main-ion poloidal flow. It is noteworthy that Eq. (2) does not contain consideration of inter-species friction between deuterium and carbon nor contributions from the Pfirsch-Schlüter viscosity contained in NCLASS (Ref. 15) which is formulated to span collisionality regimes continuously. The inconsistency between the neoclassically predicted and measured deuterium toroidal rotation evidently lies in the neoclassical prediction of the main-ion poloidal flow, or collisional friction between main ions and carbon ions.

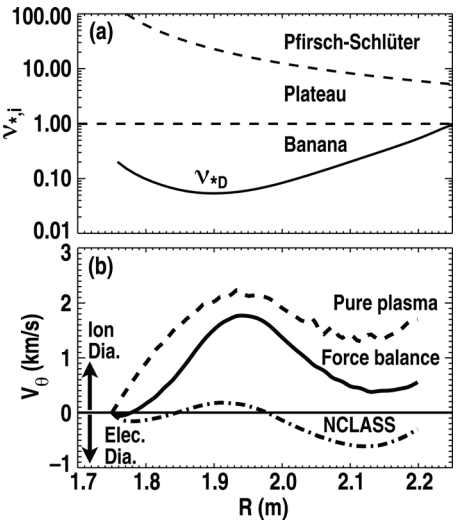

FIG. 11. Bulk ion collisionality regime and poloidal flow velocity for Fig. 8 at 2130 ms. (a) The main-ion collisionality and the three collisionality regimes. (b) Poloidal flow computed with the NCLASS code (dash-dot), force balance relation Eq. (4) (solid), and the pure plasma banana regime approximation Eq. (2) (dashed). The ion ($V_\theta > 0$) and electron diamagnetic directions are indicated.

VII. BULK ION TOROIDAL ROTATION IN THE PRESENCE OF AN INTERNAL TRANSPORT BARRIER

Plasma with strong pressure gradients are expected to exhibit the most dramatic differences between main-ion and impurity toroidal rotation. Previous work on TFTR on peculiar impurity toroidal rotation profiles which exhibited a "notch," or non-monotonic feature, asserted that the rotation profile of the main-ions should be monotonic and "notch-free."[58] In these cases, when the net torque was small but overall beam power was high, the neoclassically predicted rotation difference between carbon and deuterium exceeded 100 km/s. In order to assess the main-ion toroidal rotation in the presence of a strong pressure gradient, core transport barrier (ITB) discharges in DIII-D were executed specifically at near-balanced input torque from co-I_p and ctr-I_p neutral beams. Early NBI was used to maintain an elevated q. Figures 12(a) and 12(b) displays the evolution of q on axis, the minimum in the q profile, $q_{\min}$ and ion temperature. The grey shaded regions display core barrier formation occurring transiently near the rational minimum q crossing of $q_{\min} = 2$ at 1500 ms, briefly collapsing, only to reform as a sustained barrier approximately 25–50 ms afterwards. These two regions are identified as "$q_{\min} = 2$" and "sustained ITB" in Fig. 12.

There is little doubt that a strong pressure is contained inside of the shear reversal surface. The magnetic field strength measured by the main-ion CER system using the B-Stark technique[28–30] indicates a significant drop in the magnitude of the field, $|B|$, displayed in Fig. 13. The interpretation is similar to ion cyclotron resonance heating (ICRH) induced diamagnetism in JET.[59]

Figure 14 displays the ion temperature and toroidal rotation profiles at two times during the sustained barrier period. At 1800 ms, Fig. 14(a), the ion temperature gradient is at its

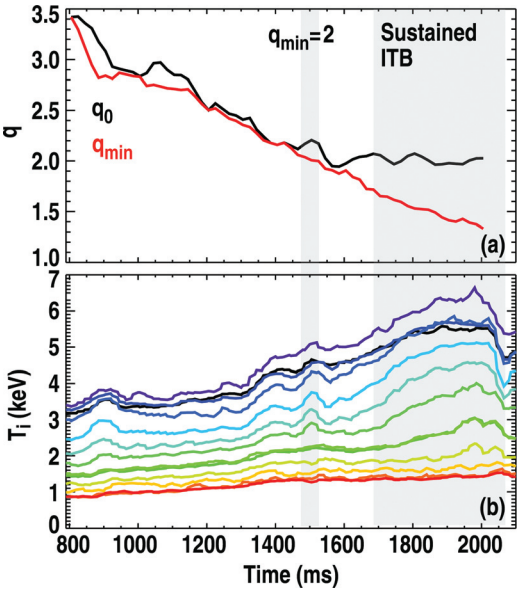

FIG. 12. (a) Safety factor value at the magnetic axis q_0 and minimum safety factor $q_{\min}$. Periods where $q_0 > q_{\min}$ indicate reversed central magnetic shear. (b) Ion temperature evolution displaying core barrier formation when the central magnetic shear is reversed. (a) and (b) Times of rational $q_{\min} = 2$ crossing and sustained reversed shear are indicated by shaded region.

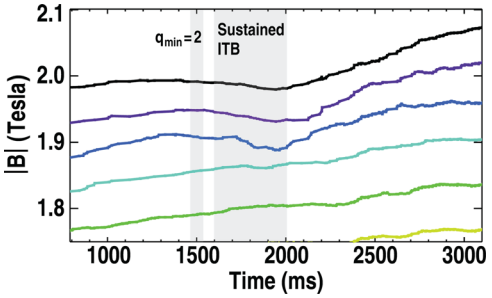

FIG. 13. Time history of magnetic field strength $|B|$ measured by the main-ion CER diagnostic displaying the strong modification to the magnetic equilibrium when there is significant plasma pressure. Lines are six time traces from measurements at major radius 1.71 m to 2.05 m.

maximum of approximately −16 keV/m. The carbon and deuterium temperatures are in reasonable agreement over most of the profile, except the points near the magnetic axis. There may be an "isotope effect"[60,61] occurring near $R \approx 1.85$ m where the ion-ion collision time is nearly 20 ms. Near the magnetic axis, the beam ion density is maximized and can couple more strongly to the higher Z carbon ions, resulting in a slightly higher temperature. However, points in the strong gradient region, $R = 1.9 - 2.1$ m are in good agreement. The carbon toroidal velocity profile in Fig. 14(a) displays a high velocity in the core, slight "notch" feature near $R = 1.95$ m, and relatively flat profile across much of minor radius. There is an additional notch at the H-mode pedestal where deuterium measurements are not available. The deuterium rotation measurements displayed in Fig. 14(a) are systematically more ctr-I_p than the carbon measurements, qualitatively similar to the intrinsic rotation measurements displayed in Sec. VI. With a strong temperature gradient and relatively weak "notch" in the carbon rotation profile, the neoclassically predicted deuterium rotation profile from NCLASS is sufficiently different from the carbon profile to remove the notch feature. However, the deuterium rotation measurements do not match the neoclassical prediction. It is of note that the *apparent* velocity (not shown) of the co-I_p views are only near the carbon measurements and the *apparent* velocity of the ctr-I_P views are significantly more counter-current, and the difference between the two views scales with T_i. The sign and magnitude of the cross section corrections are in agreement with the scaling of Fig. 7 and modeling by FIDAsim.

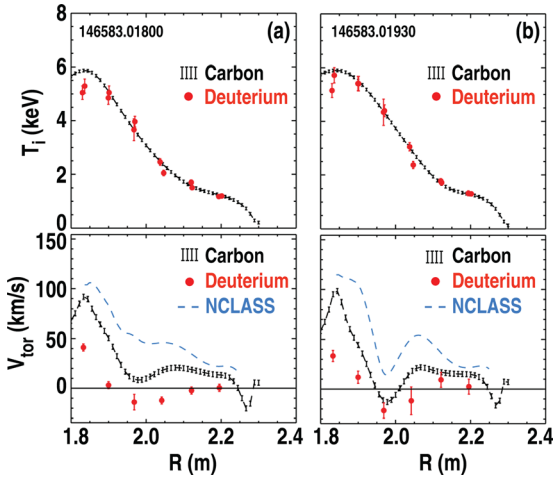

FIG. 14. Profiles of ion temperature for carbon and deuterium, and toroidal rotation of carbon, deuterium, and the neoclassically predicted deuterium toroidal rotation at (a) 1800 ms and (b) 1930 ms into the discharge.

Displayed in Fig. 14(b) are the temperature and velocity profiles at 1930 ms. At this time, the temperature gradient has *weakened* to approximately −14 keV/m, but the carbon notch has become *deeper* and crosses zero velocity. This observation that the notch becomes deeper when the temperature gradient relaxes is in qualitative disagreement with the assertion that the notch is caused by the strong gradient. In Fig. 14(b), the quantitative neoclassical prediction of the deuterium toroidal rotation now displays a notch feature as well.

The presence of the rotation notch in the toroidal velocity profile of both species deserves explanation if the notch is not a neoclassical pressure gradient effect. In reversed magnetic shear discharges with significant neutral beam injection, reversed shear Alfvén eigenmodes (RSAEs) can be excited[62,63] at integer crossings in the value of q_{min}. These modes have been observed to cause significant levels of fast-ion transport and loss.[31,64] Identification of core localized Alfvén eigenmodes (AEs) in DIII-D which have little or no external magnetic signature is possible by evaluating the cross-power spectrum of two interferometer chords. Displayed in Figs. 15(a) and 15(b) is a Fourier spectrogram of the crosspower between vertical and radial CO_2 interferometer chords, and associated power integrated between 90–160 kHz. Figure 15(c) displays the time evolution of the toroidal rotation at eight CER sightlines across the plasma radius. In Fig. 15(c), the existence of a "notch" is indicated by times where the green trace drops below the orange trace. At 1500 ms, as q_{min} crosses 2.0, there is a clear burst of coherent AE activity in Figs. 15(a) and 15(b) observed as a frequency chirping, and increase in integrated cross-power. This is the first observation of a non-monotonic "notch" forming in the toroidal rotation profile, seen in Fig. 15(c), as there is deep core spinup and a brief notch occurring. From approximately 1525 ms to 1600 ms, there is a slight reduction in the magnitude of AE intensity, and the notch feature briefly disappears. Then, at 1600 ms, there begin a sustained series of intense AE modes, which correspond with the times of deep notching of the toroidal velocity profile.

Energetic particles modes such as Alfvén eigenmodes[64] and fishbones[65] are known to cause significant fast-ion transport. During fast ion transport or loss events, large torques can be imparted rapidly and locally to the bulk plasma as populations of energetic particles become radially displaced. The process is similar to the phenomenon of "prompt torque" delivery by fast radial current injection, described and tested in detail in Ref. 57. The result of fast-ion displacement is a torque which is *species independent*. In Ref. 57, it was confirmed that injection of co-I_p fast ions causes a co-I_p torque on the plasma. Similarly, the loss or displacement of co-I_p fast ions results in a ctr-I_p torque. Here, it is speculated that sustained AE activity can induce significant, sustained transport of fast-ions, acting as a local source of torque and driving the toroidal rotation notch in *both species*, carbon

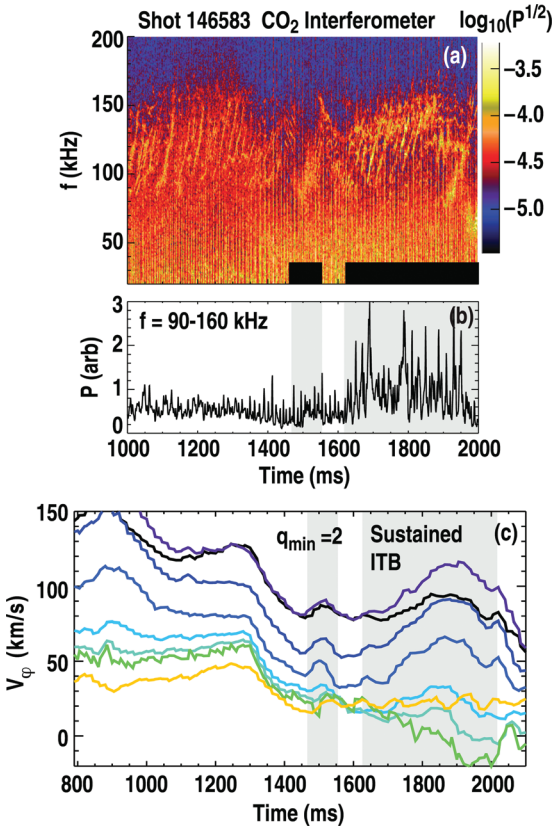

FIG. 15. (a) Spectrogram of core fluctuations displaying Alfvénic activity and (b) fluctuation power in the frequency band 90–160 kHz. (c) Time history of toroidal rotation from core to edge displaying changes in toroidal rotation coincident with coherent with strong mode amplitude. Lines in (c) are rotation measured by eight CER sightlines from core to edge. Rotation prior at 1200 ms decreases monotonically from core to edge. Shaded regions in (a)–(c) indicate $q_{\min}=2$ crossing and sustained reversed shear transport barrier.

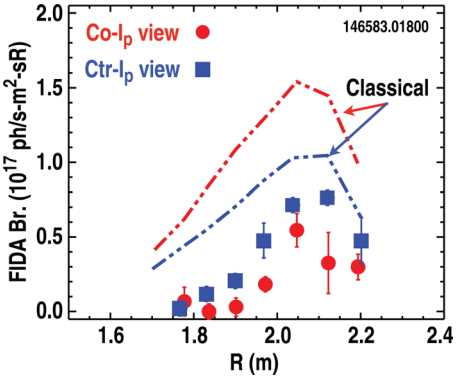

FIG. 16. Radial profile of fast-ion emission intensity FIDA at 1800 ms corresponding to Fig. 14(a). Measured FIDA emission is significantly below classical expectations indicative of fast-ion transport.

and deuterium. Furthermore, inside of a transport barrier where the thermal diffusivity χ_i is greatly reduced, and assuming that $\chi_\varphi \sim \chi_i$,[66,67] it is more likely that a sharp rotation feature can be sustained with a constant torque.

Evidence for the transport of fast ions can be seen in the profile of FIDA photoemission intensity from the main-ion CER diagnostic. Displayed in Fig. 16 is the measured fast-ion emission intensity, and classical FIDA emission intensity evaluated from FIDAsim. It is clear that the FIDA profiles (proportional to fast-ion density) are well below the classical values (compare to Fig. 4), indicating that there is significant fast-ion transport. The precise magnitude of the torque by fast-ion transport and required momentum diffusivity are the subject of ongoing calculations. It should be noted that the existence of strong Alfvén activity in TFTR discharges studied in Ref. 58 cannot be confirmed at this time.[68]

Although fast-ion transport may explain the toroidal velocity notch observed in reversed shear discharges in DIII-D, the measured main-ion toroidal rotation remains more ctr-I_p across the profile, in disagreement with the neoclassical prediction. Similar to Sec. VI B, an increased deuterium poloidal flow velocity localized to the region of steep pressure is required for consistency with the observed deuterium toroidal flow. However, it is noteworthy that neglecting the effects of a significant beam-ion population may render the direct applicability of the neoclassical theory questionable.

VIII. CONCLUSION

By exploiting the large amount of information in the active D_α spectrum, it is possible to deduce the local properties of thermal deuterium ion temperature, toroidal velocity and density, local beam emission intensity, beam neutral density and density fractions, fast ion emission intensity, and local magnetic field strength $|B|$. Corrections for atomic physics are performed by two separate methods; complementary views of co-current injected and counter-current injected neutral beams at matched major radii, and time-dependent collisional-radiative modeling of the atomic processes leading to thermal D_α emission. Both correction measurements are in qualitative and quantitative agreement.

This new main-ion measurement capability has enabled detailed studies of the bulk ion properties in deuterium fueled plasmas for the first time. Toroidal rotation measurements of both deuterium and impurity carbon are acquired simultaneously. The difference between the two ion species' toroidal rotation has been quantified and compared to neoclassical theoretical calculations. Over a range of conditions, including ECH plasmas dominated by intrinsic rotation and NBI plasmas with an internal transport barrier and steep pressure gradient, the main-ion rotation is systematically in the counter-current direction compared to carbon rotation, in significant disagreement with neoclassical theory. It is noteworthy that the collisional effects of fast ions on the two ion species may be neglected in the intrinsic rotation conditions, unlike previous impurity poloidal rotation studies which had focused on higher performance plasmas with significant populations of beam ions. The discrepancy with the neoclassical theory in the intrinsic rotation studies may lie in the neoclassical prediction of the poloidal flow, or other anomalous effects such as turbulence which is not included in the neoclassical treatment. In plasmas with an internal transport barrier, a significant notch feature was measured in the toroidal rotation of both carbon and deuterium that may be due to a counter-I_p torque from the significant fast-ion transport from Alfvén eigenmodes. It was found that a strong pressure

gradient did not drive strong differential toroidal rotation between the main-ions and carbon ions.

Further investigations into the applicability of the neoclassical theory of toroidal and poloidal flow velocity are warranted, particularly in low rotation scenarios where the contribution to the radial electric field from toroidal rotation becomes small. At low toroidal rotation, the contributions to E_r from toroidal rotation, poloidal rotation and pressure are all of the same order. Therefore, care should be taken when addressing the effects of turbulence suppression by E_r shear on transport under low rotation conditions.

ACKNOWLEDGMENTS

This work supported by the U.S. Department of Energy under DE-AC02-09CH11466, DE-FC02-04ER54698, SC-G903402, and DE-AC52-07NA27344. The author gratefully acknowledges useful discussions with R. E. Bell, E. A. Belli, J. S. deGrassie, J. A. Boedo, R. Nazikian, and M. A. Van Zeeland. The assistance of C. Chrystal is also acknowledged.

[1]A. M. Garofalo, A. D. Turnbull, M. E. Austin, J. Bialek, M. S. Chu, K. J. Comer, E. D. Fredrickson, R. J. Groebner, R. J. La Haye, L. L. Lao, E. A. Lazarus, G. A. Navratil, T. H. Osborne, B. W. Rice, S. A. Sabbagh, J. T. Scoville, E. J. Strait, and T. S. Taylor, Phys. Rev. Lett. **82**, 3811 (1999).
[2]J. W. Berkery, S. A. Sabbagh, H. Reimerdes, R. Betti, B. Hu, R. E. Bell, S. P. Gerhardt, J. Manickam, and M. Podestà, Phys. Plasmas **17**, 082504 (2010).
[3]P. A. Politzer, C. C. Petty, R. J. Jayakumar, T. C. Luce, M. R. Wade, J. C. DeBoo, J. R. Ferron, P. Gohil, C. T. Holcomb, A. W. Hyatt, J. Kinsey, R. J. La Haye, M. A. Makowski, and T. W. Petrie, Nucl. Fusion **48**, 075001 (2008).
[4]R. J. Buttery, R. J. La Haye, P. Gohil, G. L. Jackson, H. Reimerdes, E. J. Strait, and the DIII-D Team, Phys. Plasmas **15**, 056115 (2008).
[5]R. J. La Haye, D. P. Brennan, R. J. Buttery, and S. P. Gerhardt, Phys. Plasmas **17**, 056110 (2010).
[6]K. H. Burrell, Phys. Plasmas **4**, 1499 (1997).
[7]J. S. deGrassie, J. E. Rice, K. H. Burrell, R. J. Groebner, and W. M. Solomon, Phys. Plasmas **14**, 056115 (2007).
[8]J. E. Rice, A. Ince-Cushman, J. S. deGrassie, L.-G. Eriksson, Y. Sakamoto, A. Scarabosio, A. Bortolon, K. H. Burrell, B. P. Duval, C. Fenzi-Bonizec, M. J. Greenwald, R. J. Groebner, G. T. Hoang, Y. Koide, E. S. Marmar, A. Pochelon, and Y. Podpaly, Nucl. Fusion **47**, 1618 (2007).
[9]W. M. Solomon, K. H. Burrell, J. S. deGrassie, J. A. Boedo, A. M. Garofalo, R. A. Moyer, S. H. Muller, C. C. Petty, and H. Reimerdes, Nucl. Fusion **51**, 073010 (2011).
[10]R. V. Budny, R. Andre, G. Bateman, F. Halpern, C. E. Kessel, A. Kritz, and D. McCune, Nucl. Fusion **48**, 075005 (2008).
[11]R. C. Isler, Plasma Phys. Controlled Fusion **36**, 171 (1994).
[12]R. P. Seraydarian, K. H. Burrell, N. H. Brooks, R. J. Groebner, and C. Kahn, Rev. Sci. Instrum. **57**, 155 (1986).
[13]S. P. Hirshman and D. J. Sigmar, Nucl. Fusion **21**, 1079 (1981).
[14]Y. Kim, P. Diamond, and R. Groebner, Phys. Fluids B: Plasma Phys. **3**, 2050 (1991).
[15]W. A. Houlberg, K. C. Shaing, S. P. Hirshman, and M. C. Zarnstorff, Phys. Plasmas **4**, 3230 (1997).
[16]B. A. Grierson, K. H. Burrell, W. M. Solomon, and N. A. Pablant, Rev. Sci. Instrum. **81**, 10D735(2010).
[17]W. W. Heidbrink, Comm. Comput. Phys. **10**(3), 716 (2011).
[18]J. L. Luxon *et al*., Fusion Sci. Technol. **48**, 807 (2002).
[19]W. M. Solomon, K. H. Burrell, R. Feder, A. Nagy, P. Gohil, and R. J. Groebner, Rev. Sci. Instrum. **79**, 10F531 (2008).
[20]R. B. Howell, R. J. Fonck, R. J. Knize, and K. P. Jaehnig, Rev. Sci. Instrum. **59**, 1521 (1988).
[21]M. von Hellermann, P. Breger, J. Frieling, R. Konig, W. Mandl, A. Maas, and H. P. Summers, Plasma Phys. Controlled Fusion **37**, 71 (1995).
[22]R. E. Bell and E. J. Synakowski, AIP Conf. Proc. **547**, 39 (2000).
[23]R. E. Bell and R. Feder, Rev. Sci. Instrum. **81**, 10D724 (2010).
[24]W. M. Solomon, K. H. Burrell, P. Gohil, R. J. Groebner, and L. R. Baylor, Rev. Sci. Instrum. **75**, 3481 (2004).
[25]D. M. Thomas, G. R. McKee, K. H. Burrell, F. Levinton, E. L. Foley, and R. K. Fisher, Fusion Sci. Technol. **53**, 487 (2008).
[26]W. Mandl, Technical Report JET-IR(92)05, JE-T, 1992.
[27]J. T. Hogan, J. Nucl. Mater. **111**, 413 (1982).
[28]N. A. Pablant, K. H. Burrell, R. J. Groebner, D. H. Kaplan, and C. T. Holcomb, Rev. Sci. Instrum. **79**, 10F517 (2008).
[29]N. A. Pablant, K. H. Burrell, R. J. Groebner, C. T. Holcomb, and D. H. Kaplan, Rev. Sci. Instrum. **81**, 10D729 (2010).
[30]N. A. Pablant, Ph.D dissertation, University of California, San Diego, 2010).
[31]W. W. Heidbrink, N. N. Gorelenkov, Y. Luo, M. A. Van Zeeland, R. B. White, M. E. Austin, K. H. Burrell, G. J. Kramer, M. A. Makowski, G. R. McKee, R. Nazikian, and the DIII-D Team, Phys. Rev. Lett. **99**, 245002 (2007).
[32]W. W. Heidbrink, J. M. Park, M. Murakami, C. C. Petty, C. Holcomb, and M. A. Van Zeeland, Phys. Rev. Lett. **103**, 175001 (2009).
[33]R. J. Hawryluk, in *Physics of plasmas close to thermonuclear conditions*, edited by B. Coppi, G. G. Leotta, D. Pfirsch, R. Pozzoli, and E. Sindoni (CEC/Pergamon, Brussels, 1980), Vol. 1, p. 19.
[34]R. J. Goldston, D. C. McCune, H. H. Towner, S. L. Davis, R. J. Hawryluk, and G. L. Schmidt, J. Comput. Phys. **43**, 61 (1981).
[35]A. Pankin, D. McCune, R. Andre, G. Bateman, and A. Kritz, Comput. Phys. Commun. **159**, 157 (2004).
[36]L. L. Lao, H. St. John, R. D. Stambaugh, A. G. Kellman, and W. Pfeiffer, Nucl. Fusion **25**, 1611 (1985).
[37]Y. Luo, W. W. Heidbrink, K. H. Burrell, E. Ruskov, and W. M. Solomon, Phys. Plasmas **14**, 112503 (2007).
[38]W. Mandl, R. C. Wolf, M. G. von Hellermann, and H. P. Summers, Plasma Phys. Controlled Fusion **35**, 1373 (1993).
[39]See http://www.adas.ac.uk for ADAS atomic data and analysis structure. The originating developer of ADAS is the JET joint undertaking.
[40]O. Marchuk, Y. Ralchenko, R. K. Janev, W. Biel, E. Delabie, and A. M. Urnov, J. Phys. B: Atomic, Molecular and Optical Physics **43**, 011002 (2010).
[41]J. A. Boedo, E. A. Belli, E. Hollmann, W. M. Solomon, D. L. Rudakov, J. G. Watkins, R. Prater, J. Candy, R. J. Groebner, K. H. Burrell, J. S. deGrassie, C. J. Lasnier, A. W. Leonard, R. A. Moyer, G. D. Porter, N. H. Brooks, S. Muller, G. Tynan, and E. A. Unterberg, Phys. Plasmas **18**, 032510 (2011).
[42]S. H. Müller, J. A. Boedo, K. H. Burrell, J. S. deGrassie, R. A. Moyer, D. L. Rudakov, and W. M. Solomon, Phys. Rev. Lett. **106**, 115001 (2011).
[43]S. H. Müller, J. A. Boedo, K. H. Burrell, J. S. deGrassie, R. A. Moyer, D. L. Rudakov, W. M. Solomon, and G. R. Tynan, Phys. Plasmas **18**, 072504 (2011).
[44]P. Helander and D. J. Sigmar, *Collisional Transport in Magnetized Plasmas*, edited by M. G. Haines *et al*. (Cambridge University Press, Cambridge, MA, 2002).
[45]J. Kim, K. H. Burrell, P. Gohil, R. J. Groebner, Y.-B. Kim, H. E. St. John, R. P. Seraydarian, and M. R. Wade, Phys. Rev. Lett. **72**, 2199 (1994).
[46]W. M. Solomon, K. H. Burrell, R. Andre, L. R. Baylor, R. Budny, P. Gohil, R. J. Groebner, C. T. Holcomb, W. A. Houlberg, and M. R. Wade, Phys. Plasmas **13**, 056116 (2006).
[47]R. E. Bell, R. Andre, S. M. Kaye, R. A. Kolesnikov, B. P. LeBlanc, G. Rewoldt, W. X. Wang, and S. A. Sabbagh, Phys. Plasmas **17**, 082507 (2010).
[48]A. R. Field, J. McCone, N. J. Conway, M. Dunstan, S. Newton, and M. Wisse, Plasma Phys. Controlled Fusion **51**, 105002 (2009).
[49]R. E. Bell, F. M. Levinton, S. H. Batha, E. J. Synakowski, and M. C. Zarnstorff, Phys. Rev. Lett. **81**, 1429 (1998).
[50]K. Crombé, Y. Andrew, M. Brix, C. Giroud, S. Hacquin, N. C. Hawkes, A. Murari, M. F. F. Nave, J. Ongena, V. Parail, G. Van Oost, I. Voitsekhovitch, and K.-D. Zastrow, Phys. Rev. Lett. **95**, 155003 (2005).
[51]E. A. Belli and J. Candy, Plasma Phys. Controlled Fusion **50**, 095010 (2008).
[52]W. X. Wang, W. M. Tang, F. L. Hinton, L. E. Zakharov, R. B. White, and J. Manickam, Comput. Phys. Commun. **164**, 178 (2004).
[53]R. E. Waltz, G. M. Staebler, J. Candy, and F. L. Hinton, Phys. Plasmas **14**, 122507 (2007).
[54]G. Dif-Pradalier, P. H. Diamond, V. Grandgirard, Y. Sarazin, J. Abiteboul, X. Garbet, P. Ghendrih, G. Latu, A. Strugarek, S. Ku, and C. S. Chang, Phys. Plasmas **18**, 062309 (2011).
[55]J. E. Rice, M. Greenwald, I. H. Hutchinson, E. S. Marmar, Y. Takase, S. M. Wolfe, and F. Bombarda, Nucl. Fusion **38**, 75 (1998).
[56]J. S. deGrassie, R. J. Groebner, K. H. Burrell, and W. M. Solomon, Nucl. Fusion **49**, 085020 (2009).

[57]J. S. deGrassie, R. J. Groebner, and K. H. Burrell, Phys. Plasmas **13**, 112507 (2006).
[58]D. R. Ernst, M. G. Bell, R. E. Bell, C. E. Bush, Z. Chang, E. Fredrickson, L. R. Grisham, K. W. Hill, D. L. Jassby, D. K. Mansfield, D. C. McCune, H. K. Park, A. T. Ramsey, S. D. Scott, J. D. Strachan, E. J. Synakowski, G. Taylor, M. Thompson, and R. M. Wieland, Phys. Plasmas **5**, 665 (1998).
[59]R. C. Wolf, L.-G. Eriksson, M. Von Hellermann, R. König, W. Mandl, and F. Porcelli, Nucl. Fusion **33**, 1835 (1993).
[60]H. Eubank, R. Goldston, V. Arunasalam, M. Bitter, K. Bol, D. Boyd, N. Bretz, J.-P. Bussac, S. Cohen, P. Colestock, S. Davis, D. Dimock, H. Dylla, P. Efthimion, L. Grisham, R. Hawryluk, K. Hill, E. Hinnov, J. Hosea, H. Hsuan, D. Johnson, G. Martin, S. Medley, E. Meservey, N. Sauthoff, G. Schilling, J. Schivell, G. Schmidt, F. Stauffer, L. Stewart, W. Stodiek, R. Stooksberry, J. Strachan, S. Suckewer, H. Takahashi, G. Tait, M. Ulrickson, S. von Goeler, and M. Yamada, Phys. Rev. Lett. **43**, 270 (1979).
[61]R. V. Budny, M. G. Bell, H. Biglari, M. Bitter, C. E. Bush, C. Z. Cheng, E. D. Fredrickson, B. Grek, K. W. Hill, H. Hsuan, A. C. Janos, D. L. Jassby, D. W. Johnson, L. C. Johnson, B. LeBlanc, D. C. McCune, D. R. Mikkelsen, H. K. Park, A. T. Ramsey, S. A. Sabbagh, S. D. Scott, J. F. Schivell, J. D. Strachan, B. C. Stratton, E. J. Synakowski, G. Taylor, M. C. Zarnstorff, and S. J. Zweben, Nucl. Fusion **32**, 429 (1992).
[62]H. Berk, D. Borba, B. Breizman, S. Pinches, and S. Sharapov, Phys. Rev. Lett. **87**, 185002 (2001).
[63]R. Nazikian, N. N. Gorelenkov, B. Alper, H. L. Berk, D. Borba, R. V. Budny, G. Y. Fu, W. W. Heidbrink, G. J. Kramer, M. A. Makowski, S. D. Pinches, S. E. Sharapov, W. M. Solomon, E. J. Strait, R. B. White, M. A. Van Zeeland, and JET-EFDA Contributors, Phys. Plasmas **15**, 056107 (2008).
[64]M. A. Van Zeeland, W. W. Heidbrink, R. K. Fisher, M. G. Muñoz, G. J. Kramer, D. C. Pace, R. B. White, S. Aekaeslompolo, M. E. Austin, J. E. Boom, I. G. J. Classen, S. da Graca, B. Geiger, M. Gorelenkova, N. N. Gorelenkov, A. W. Hyatt, N. Luhmann, M. Maraschek, G. R. McKee, R. A. Moyer, C. M. Muscatello, R. Nazikian, H. Park, S. Sharapov, W. Suttrop, G. Tardini, B. J. Tobias, Y. B. Zhu, and DIII-D and ASDEX Upgrade Teams, Phys. Plasmas **18**, 056114 (2011).
[65]W. W. Heidbrink, M. E. Austin, R. K. Fisher, M. García-Muñoz, G. Matsunaga, G. R. McKee, R. A. Moyer, C. M. Muscatello, M. Okabayashi, D. C. Pace, K. Shinohara, W. M. Solomon, E. J. Strait, M. A. Van Zeeland, and Y. B. Zhu, Plasma Phys. Controlled Fusion **53**, 085028 (2011).
[66]J. S. deGrassie, D. R. Baker, K. H. Burrell, P. Gohil, C. M. Greenfield, R. J. Groebner, and D. M. Thomas, Nucl. Fusion **43**, 142 (2003).
[67]P. C. de Vries, M.-D. Hua, D. C. McDonald, C. Giroud, M. Janvier, M. F. Johnson, T. Tala, K.–D. Zastrow, and JET EFDA Contributors, Nucl. Fusion **48**, 1 (2008).
[68]D. Ernst, private communication (2011).